



A study of intracortical porosity's area fractions and aspect ratios using computer vision and pulse-coupled neural networks

Ilige S. Hage¹ · R. F. Hamade²

Received: 11 May 2018 / Accepted: 14 September 2018 / Published online: 28 September 2018
© International Federation for Medical and Biological Engineering 2018

Abstract

Employing computer vision (CV) and optimized pulse-coupled neural networks (PCNN), this work automatically quantifies the geometrical attributes of intracortical bone porosity (namely lacunae and canaliculi (L-C), Haversian canals, and resorption cavities). Fifty pathological slides of cortical bone ($\times 20$ magnification) were prepared from middiaphysis of bovine forelegs collected fresh from butcher. Biopsies were subdivided into sectors encircling arcs (θ of 10°) and radial distances (R) originating from the bone's geometric center toward posterior regions and spanning 3.3 mm. Microscopically, each pore is classified according to whether it belonged to primary or secondary osteon. Globally, each pore is assigned as being located in anterior or posterior regions. For each pore, area and major/minor axes lengths were determined as raw measures from which derived geometric measures, namely, area fraction (AF) and aspect ratio (AR), were derived. Said measures were plotted versus R (for different angles). Plots of AF and AR trends were found to vary linearly along the radial distance. Area fractions (%) significantly decreased linearly with R ($p < 0.01$) in the anterior region. In the posterior region, area fraction values are flat versus R . These findings are indicative of maturing osteons at the outer cortex with predominately near circular-shaped pores.

Keywords Computer vision · Pulse-coupled neural networks · Automatic segmentation · Cortical porosity · Area fraction · Aspect ratio

Nomenclature

$\%so$	% area of secondary osteons in image
$\%po$	% area of primary osteons in image
A_{so}	Area of secondary osteons in image
A_{po}	Area of primary osteons in image
A_{rc}	Area of resorption cavity(ies) in image
$S(A_{so}^l)$	Summed areas of lacunae in secondary osteons in image
$S(A_{po}^l)$	Summed areas of lacunae in primary osteons in image
$S(A_{so}^c)$	Summed areas of canaliculi clusters in secondary osteons in image

$S(A_{po}^c)$	Summed areas of canaliculi clusters in primary osteons in image
$S(A_{so}^{hc})$	Summed areas of Haversian canals in secondary osteons in image
AF_{so}^l	Area fraction (%) of lacunae in secondary osteons in image
AF_{po}^l	Area fraction (%) of lacunae in primary osteons in image
AF_{so}^c	Area fraction (%) of canaliculi clusters in secondary osteons in image
AF_{po}^c	Area fraction (%) of canaliculi clusters in primary osteons in image
AF_{so}^{hc}	Area fraction (%) of Haversian canals in secondary osteons in image
AF^{rc}	Area fraction (%) of resorption cavity(ies) in image

✉ R. F. Hamade
rh13@aub.edu.lb

Ilige S. Hage
ilige.hage@ndu.edu.lb

¹ Department of Mechanical Engineering, Notre Dame University-Louaize, Zouk Mosbeh, P.O. Box: 72, Zouk Mikael, Lebanon

² Department of Mechanical Engineering, American University of Beirut, Riad El-Solh, Beirut 1107 2020, Lebanon

1 Introduction

Despite the advent of such relatively new procedures as electron (scanning and transmission) microscopy, magnetic

resonance, micro-scale-capable radiography, and computed tomography, light microscopy remains a well-practiced method utilized medically as part of restorative picture examination. Examining and measuring porosity microarchitecture in human and animal cortical bone, particularly as applied to bone pathology, has been (Remaggi et al. [1]) and continues to be of much interest (Cardoso et al. [2]). In the osteonal bone microstructure, cortical porosity constitutes of relatively large-sized pores (mainly vascular or Haversian porosity (VP) and resorption cavities) and of the finer network of pores in the mineralized matrix consisting of the lacunar-canalicular porosity (LCP). Many quantitative studies of cortical porosity (defined as total pore area divided by cortical bone area) report on aggregate porosity without attempting to classify porosity according to (1) whether vascular porosity or lacunar-canalicular porosity or (2) to whether pore is located within primary or secondary osteons.

There is lack of reporting related to the quantification of the area and shape of the pores due to resolution limitations or digital processing complexity. While vascular porosity measure upwards of 50 μm , the osteocyte lacunar pores and thin canalicular channels constituting the LCP network are of characteristic sizes of the order of a few microns making these features hard to distinguish not to mention their quantification. In order to overcome resolution issues, Wang and Ni [3] had to employ low-field pulsed NMR as a technique adept for resolving micron-sized features such as lacunae. Lin and Xu [4] employed atomic force microscopy (AFM) to measure auxiliary data of demineralized compact bone from bovine tibia. Numerous strategies (e.g., X-ray) do not have the ability to determine LCP's fine structures with studies reporting aggregate quantitative porosity values extracted mostly from vascular porosity (VP) features.

Thomas et al. [5] used X-ray microradiographs to study patterns of overall porosity distribution in the midshaft of the human femur. The study utilized microradiographs of areas of cortex isolated radially into three rings and into octants circumferentially. Results showed that the inner part of the cortex is more porous than the outer parts. Thomas et al. [6] conducted further studies that demonstrated that mean pore areas progressively increase from the outer circumferential lamella toward the endosteal. However, there is lack of reported research on discerning geometrical difference in vascular (Haversian canal) and lacunar-canalicular pores' size and shape between anterior and posterior regions or according to whether the pores are located within secondary or primary osteons of cortical bone. However, in order to resolve this research question, many digital segmentation and quantification has to be brought to bear on this problem.

Earlier noninvasive quantification is using computed tomography (CT). Bousson et al. [7] used 100- μm -thick transverse (perpendicular to the femoral axis) CT sections to study the distribution of the porosity in the human femoral cortex

based on periosteal, midcortical, and endosteal cortical sub-regions. Their work covered the combined sizes of pores with average value of intraspecimen mean pore size for the entire cortical width revealing mean values of 72 and 78 μm , respectively. Perhaps due to the limited resolution, no distinction was reported amongst VP and LCP. Noninvasive quantification of in vivo cortical bone microstructure was also made possible via employing micro-CT (μCT), the gold standard for bone microarchitecture quantification, or the more recent development of high-resolution peripheral quantitative computed tomography (HR-pQCT). Recently, and for the same purpose, Nirody et al. [8] used in vivo high-resolution peripheral quantitative computed tomography (HR-pQCT) to compute three metrics: total pore area, total pore number count, and average pore area. The calculation plan of cortical porosity in Nirody et al. depended on work by Tjong et al. [9] by which a skeletonization routine deconstructed the cortical pore network into singular components. However, with their reported voxel sizes of 18 μm and 41 μm for μCT and HR-pQCT, respectively, quantification of cortical porosity % area would be only possible for relatively large mico-features such as Haversian canals. For many other substantially smaller mico-features (e.g., lacuna and canalucli), such noninvasive techniques may not be employable. Furthermore, attempting to quantify additional salient attributes of these features such as their shape or aspect ratio would prove futile. Burghardt et al. [10] needed to discard pores of size under 5 voxels in order to measure porosity in cortical bone microarchitecture of the distal radius and tibia by HR-pQCT.

Earlier works of collective cortical bone porosity tend to report mean or aggregate attributes of porosity with most techniques being incapable of resolving and segregating such fine-sized LCP features. Another challenge that this study aims to remedy is the challenge of automation where only handful of works employ automation to quantify the salient characteristics of LCP (e.g., aspect ratio) not to mention the distribution of such fine pores across the cortical thickness. In an attempt to automate the process of analyzing intracortical porosity in human femoral bone, Stein et al. [11] employed an automated image acquisition and analysis system of microradiographs and camera images of sections cut from human femoral midshaft. However, osteocyte lacunae are beneath the lower furthest reaches of recognition of the mechanized framework. A statement was recorded that highlighted the difficulties associated with characterizing the LCP. Therefore, combining automation and fine resolution in order to quantify such attributes is the major contribution of this work where light microscopy utilizing histology slides from cross sections from bovine (cow) middiaphysis cortical bone are employed. High fidelity automated segmentation is based on recent works by Hage and Hamade [12–16] as will be briefly explained. Automated segmentation is utilized where for each image, individual pores are discerned and separated. Values of area

fraction (AF) and aspect ratio (AR) for each type of pore, namely, lacunae, clusters of canaliculi network, Haversian canals, and resorption cavities, are extracted. The automated methodology allowed for the processing of large number of images with minimal human intervention. An additional contribution is the plotting of the findings (area fraction and aspect ratio values) for VP and LCP across cortical thickness as function of the radius, R , emanating from bone center. Quantitative findings suggest that intracortical bone porosities exhibit significantly varying distributions along the midcortical regions of the femur's midshaft. Plotted results indicate maturing osteonic trends in the regions closer to the outer cortex of the bone.

2 Methods

2.1 Processing of bone biopsies

Cortical femur bone biopsies (from 2-year-old bovine cow gathered straight from a butcher) are gathered from the middiaphysis due to simplicity of clinical accessibility. Bones followed laboratory processing starting by fixation in formalin to decalcifying and finishing by staining utilizing H&E solutions important for identifying unique highlights (Revell [17]). From the decalcified bone, 2-mm-thick cortex slices got dried out and paraffin-covered in Leica machine model 300 followed by slicing using a rotary microtome (model 340 E microm). Slices are then rehydrated with hot water and exposed to Hematoxylin and Eosin (H&E) staining solution to enhance visualization. Optical slides are collected from posterior (outer circumferential lamella) and anterior (midcortical) locations similar to Thomas et al. [5, 6] using light microscopy.

2.2 Histology image acquisition

For each pathologically treated biopsy, about 50 images are captured at $\times 20$ (5 images at $\times 5$ are gridded into 25 images at $\times 20$); about 50 of which (at $\times 20$) are selected in the study per biopsy. Figure 1 is a collage of illustrations, images, and magnified and processed images obtained of biopsies from bone 1 (left) and bone 2 (right). Figure 1(a) is an illustration of cortical bone section (from femur) highlighting the 3 regions: outer circumferential lamella, midcortical, and endocortical. The imaged histology area of interest is about 2.5 mm \times 3 mm located near the cortex and bound by a 10° arc from bone center (see Fig. 1(b), (c)). Optical images of slices were acquired using an Olympus BX-41 M LED optical microscope using an Olympus SC30 digital microscope camera (based on a 3.3-megapixel CCD chip with a CMOS color sensor). Figure 1 contains actual images for bone biopsies (left) 1 and (right) 2. Actual sections are shown in Fig. 1(b) with

center of the bone and reference polar coordinate system (R/Θ) illustrating angular and radial coordinates. Figure 1(c) shows biopsies' location within the sections. Figure 1(d) shows stained bone biopsies with actual optical slides ($\times 5$). Figure 1(e) shows example slides at $\times 20$ magnification. (Some of this content is copied from the conference paper Proceedings of the World Congress on Engineering 2014 Vol I, WCE 2014, July 2–4, 2014, London, U.K.).

Figure 2 shows the images ($\times 20$) used in the segmentation work. These are a larger version of those shown in Fig. 1(d). Images taken at $\times 5$ are gridded into 25 images where each of these images is later captured at $\times 20$ for better resolution. In Fig. 2 (top) of bone 1 and Fig. 2 (bottom) of bone 2, the dotted lines identify the group of 25 images captured at $\times 20$. Demarcation lines are traced by hand to separate anterior from posterior regions. Computer best-fitted arc-radii of demarcation lines are placed to simplify the segmentation analysis (marked at R5 (16 mm) for bone 1 and R4 (16.4 mm) for bone 2 as sketched in Fig. 2. Segmentation of pores will reveal the predominant pores (and their area fractions, %) of the microstructures within each region.

In Fig. 1(b), a polar coordinate system is adopted to find the location of the bone micro-constituents. The distance between the origin and the inner diameter of the bone (Fig. 1(b)) is measured using digital calipers to be 12 mm (12,000 μm) for bone 1 and 12.6 mm (12,600 μm) for bone 2. To the outer diameter, distances of 18.2 mm and 19 mm are measured for bones 1 and 2, respectively.

The $\times 20$ images are localized and oriented using the Cartesian coordinate (x - y) system by exploiting the calibrated scale bar of the microscope image as shown in Fig. 3 (left: bone 1, right: bone 2). Utilizing Cartesian-to-polar coordinate transformations, polar coordinates for the center of each image is calculated and each image is selected corresponding radial and angle coordinates. The center of each of the $\times 20$ images is located and radial distance from bone center and polar angle values are assigned to each center. Depicted on Fig. 3 are optical slides that fall along the same angle and/or same radius.

2.3 Microstructure automatic segmentation

Each of the $\times 20$ magnification images is divided into four images using PCNN-PSO-AT methodology developed by the authors (Hage and Hamade [12]). Pore shape is treated via the aspect ratio (AR) attribute defined as the ratio of minor axis length/major axis length of an ellipse shape to which each pore is automatically best fitted. Percent porosity of total area (here, area fraction (%)) (AF) is the attribute utilized to account for pores' size. The variation of these two attributes is plotted over 3.3 mm in radial length. To get an appreciation for the amount of processing work, the following pores had to be segmented: 462 Haversian canals, total of 39,600 lacunae

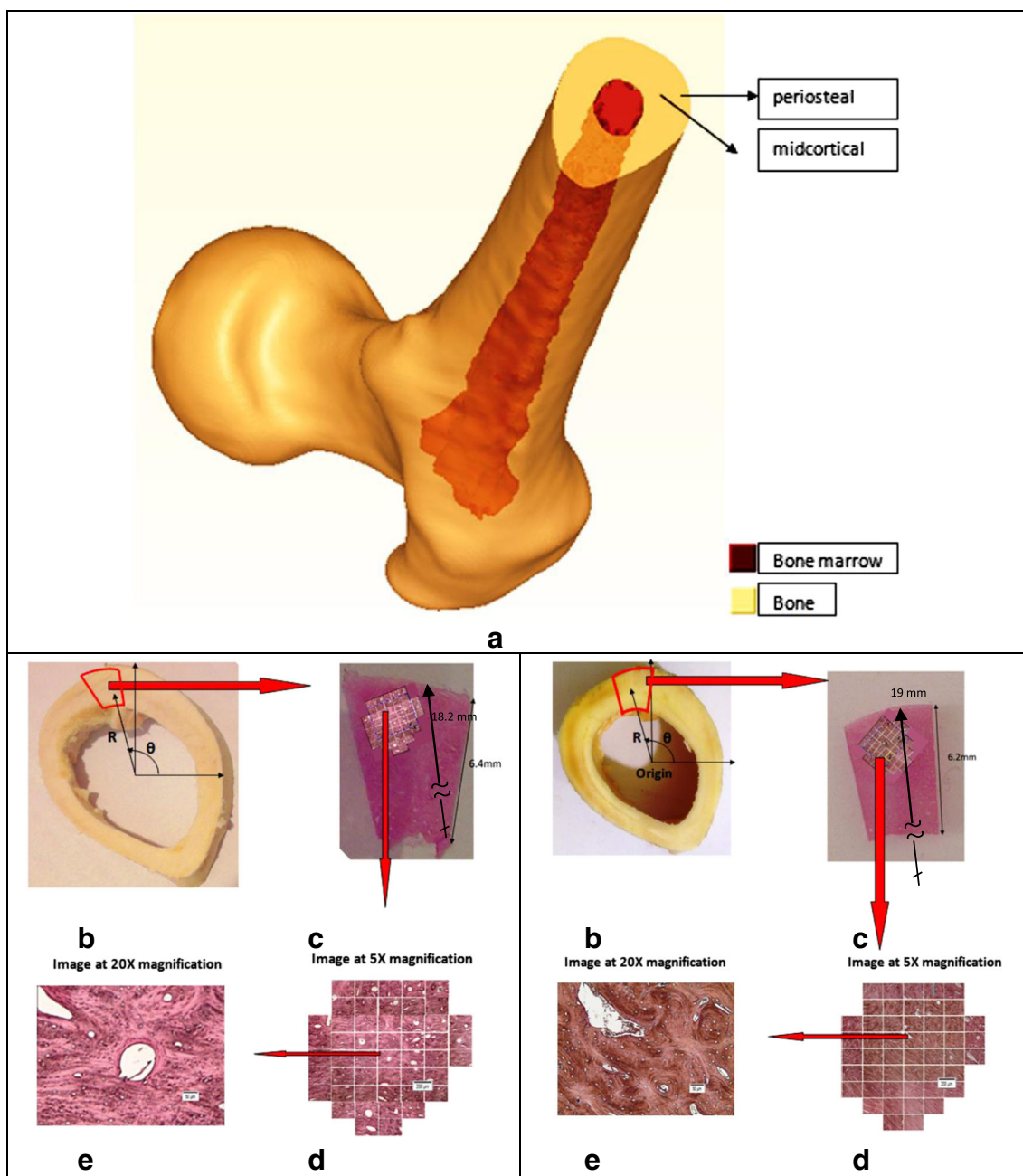


Fig. 1 (Left: bone 1; right: bone 2) a) illustration showing periosteal and midcortical regions of cortical bone, b) cut section with polar coordinates, c) location of pathologically processed biopsy within section, d) optical slides ($\times 5$) within biopsy, and e) example image ($\times 20$)

(17,963 inside secondary osteons; 21,637 in primary osteons), and 3,354,488 canaliculi (462,500 in secondary osteons and 2,891,988 in primary osteons). All pores, most of which only a few microns in size, were identified with minimal human intervention through the automated methodology.

2.3.1 Demarcation of secondary and primary osteons

The micro pores had to be assigned to their corresponding secondary and primary osteons with the revealed cement lines thus adding another 200 images of cement lines in the process (600

images total of images of lacunae, canaliculi and Haversian canals in their secondary and primary osteons). To get secondary and primary osteons mask images from the cement lines images, masks have to be created by generating 200 extra images as per the process developed by Hage and Hamade [16].

2.3.2 Image segmentation procedure

To produce binary pulses (images) representing the segmentations of the cortical porosity in bone histology, a technique based on pulse-coupled neural networks (PCNN) was recently

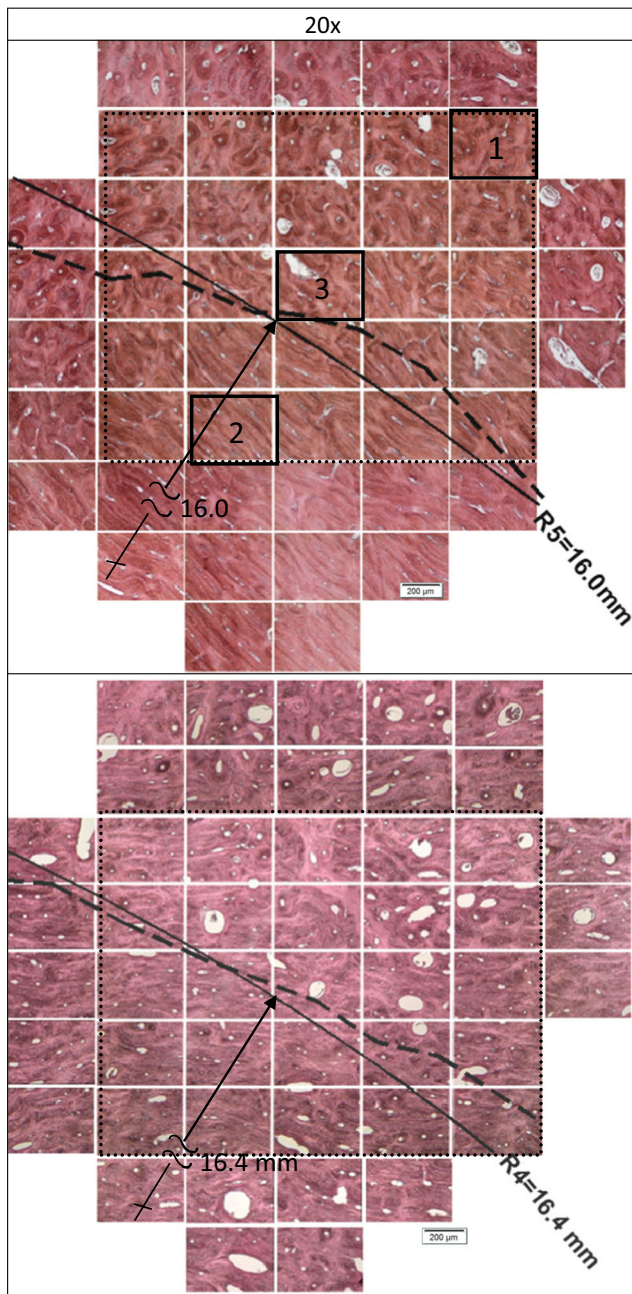


Fig. 2 (Top: bone 1; bottom: bone 2) Grids of slides where area marked with dotted lines represent a group of 25 images magnified at $\times 20$. Dashed lines represent hand-drawn demarcation lines between anterior and posterior regions. Solid lines are best-fit arc-radii ($R5 = 16$ mm for bone 1; $R4 = 16.4$ mm for bone 2). Squares 1, 2, and 3 represent the example images used

developed by Hage and Hamade [12, 14, 16]. PCNNs are unique artificially intelligent (AI) tools that model neural activity of an image (Lindblad and Kinser [18]). PCNN parameters do not self-adapt to different images requiring a hybrid combination of PCNN, particle swarm optimization (PSO), and adaptive threshold (AT) (the AT portion of the method is based on work by Gao et al. [19] to determine one set of

optimized parameters based on one image to automatically segment pores in many bone images.

All of the $\times 20$ images are segmented based on this methodology as described hereafter. The analysis takes into account the region in which such pores are located: midcortical or cortex (near periosteal surface) where Haversian-type bones are characterized by periosteal regions that contain osteons with near circular-shaped osteons and midcortical regions exhibiting compactly flattened-shaped osteons (Mayya et al. [20]). Automated segmentation has been utilized where for each image individual pores are discerned and separated. Values of AF and AR values for each type of pore, namely, lacunae, clusters of canaliculi network (since individual canals of roughly $0.5 \mu\text{m}$ in work reported in Mayya et al. [20]), could not be resolved. Based on work by Hage and Hamade [12, 16], raw parameters (measures) of geometric attributes (i.e., count, area, elliptical minor and major axes lengths) of each pore (after being individually segmented) were determined. Pores were also classified by type as Haversian, lacunae, canaliculi, or resorption pores. Consequently, determining the values of derived measures such as area fraction (AF, %) and aspect ratio (AR) of each pore located at different R/θ combinations is made possible. Processed in total were 462 Haversian canals, 39,600 lacunae (17,963 inside secondary osteons, 21,637 in primary osteons), and 3,354,488 canaliculi (462,500 in secondary osteons and 2,891,988 in primary osteons). Next, osteons are demarcated and identified osteon (primary or secondary) per cement lines (Hage and Hamade [16]). Each identified pore was assigned to an osteon (primary or secondary).

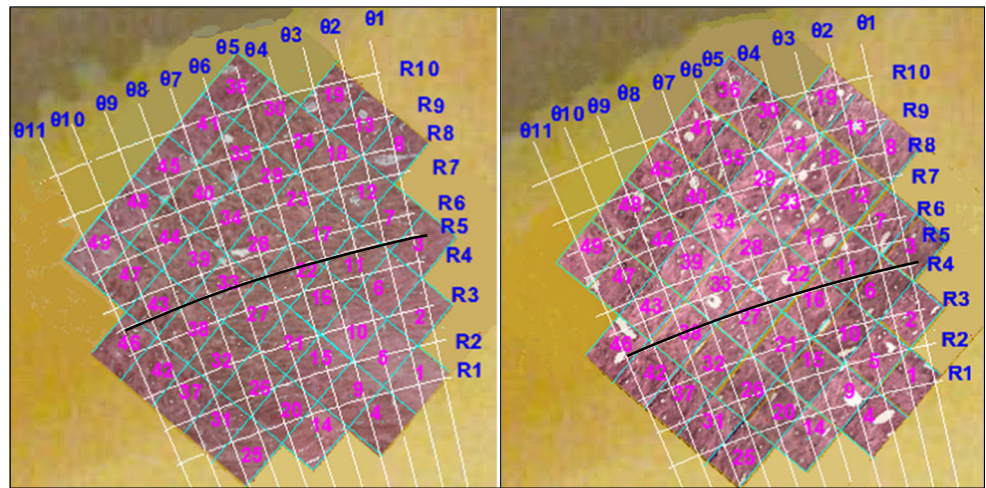
Figure 4 demonstrates the resultant segmented Haversian vascular porosity (VP), lacunae and canaliculi porosity (LCP) networks in secondary and primary osteons disambiguated along cement lines (as well as resorption cavity found in image 3). Images numbered 1, 2, and 3 correspond to the squares in Fig. 2 (bone 1) and are located at $(\theta_4 = 105^\circ; R_9 = 17.4 \text{ mm})$, $(\theta_6 = 107^\circ; R_3 = 15.3 \text{ mm})$, and $(\theta_6 = 107^\circ; R_6 = 16.3)$, respectively.

2.4 Measures and derived measures

Having segmented and demarcated the histology slides per above, the following measures were determined automatically:

1. Number counts: all segmented pores are located and counted.
2. Areas: for each individual pore, area was determined.
3. Major and minor axis length: for each individual pore, axes lengths were determined.

Fig. 3 (left: bone 1; right: bone 2) Images ($\times 20$) of bone 1 in the polar coordinate system with their respective angles and radii



Having derived raw measures, derived measures are then calculated.

4. Area fractions (AF): For each individual pore, calculate the area fraction values (AF, area of the pores/area of the corresponding osteon). Each of the 600 images is analyzed to get the values for area. Primary and secondary osteons areas have to be calculated from each of the 200 masked images.
5. Aspect ratios (AR): For each individual pore, calculate the aspect ratio (AR) values. Each of the 600 images is analyzed to determine major and minor axis length of the three different pores. Finally, data has to be sorted

based on their polar coordinates to where they can be plotted.

3 Results of derived measures of area fractions (AF) and aspect ratios (AR)

Using the methodology outlined above, data processing was conducted on two different bones extracted from two different foreleg bones of different cows where several slices are quantified and averaged resulting in two sets of data: one set for bone 1 and another for bone 2. All steps listed above were

Original image	Segments						
1	Lacunae in secondary osteons	Lacunae in primary osteons	Canaliculi clusters in secondary osteons	Canaliculi clusters in primary osteons	Haversian in secondary osteons	Cement lines	
2	Lacunae in secondary osteons	Lacunae in primary osteons	Canaliculi clusters in secondary osteons	Canaliculi clusters in primary osteons	Haversian in secondary osteons	Cement lines	
3	Lacunae in secondary osteons	Lacunae in primary osteons	Canaliculi clusters in secondary osteons	Canaliculi clusters in primary osteons	Haversian in secondary osteons	Cement lines	Resorption cavity

Fig. 4 Segmented cortical porosity: lacunae, Haversian canals, canaliculi clusters, in secondary and primary osteons, and cement lines

performed on both bones. (Although results for bone 2 were found to agree qualitatively and quantitatively with those found for bone 1, results for bone 2 were not reported here due to space limitation).

Pore shape is represented by the aspect ratio (AR) measure defined as the ratio of minor axis/major axis lengths of an ellipse shape to which each pore is automatically best fitted. Percent porosity of total area (here, area fraction, % AF) is the attribute utilized to account for pores' size. Taken separately, the number count and/or size of the pores contribute to AF. In this section, AF and AR values determined previously for all pores (in bone 1 biopsies) at combinations of R and Θ are plotted versus the radius, R . The variation of these two attributes is plotted along about 3.3 mm in radial length. (Some of the results in this section are copied from the conference paper Proceedings

of the World Congress on Engineering 2014 Vol I, WCE 2014, July 2–4, 2014, London, U.K.).

3.1 Lacunae

Lacunae' area fraction (%) values in each region are calculated by dividing the sum of lacunae areas in the secondary and primary regions by the sum of areas of said regions, respectively, according to Eqs. 1 and 2.

$$AF_{so}^l = \frac{S(A_{so}^l)}{A_{so}} \tag{1}$$

$$AF_{po}^l = \frac{S(A_{po}^l)}{A_{po}} \tag{2}$$

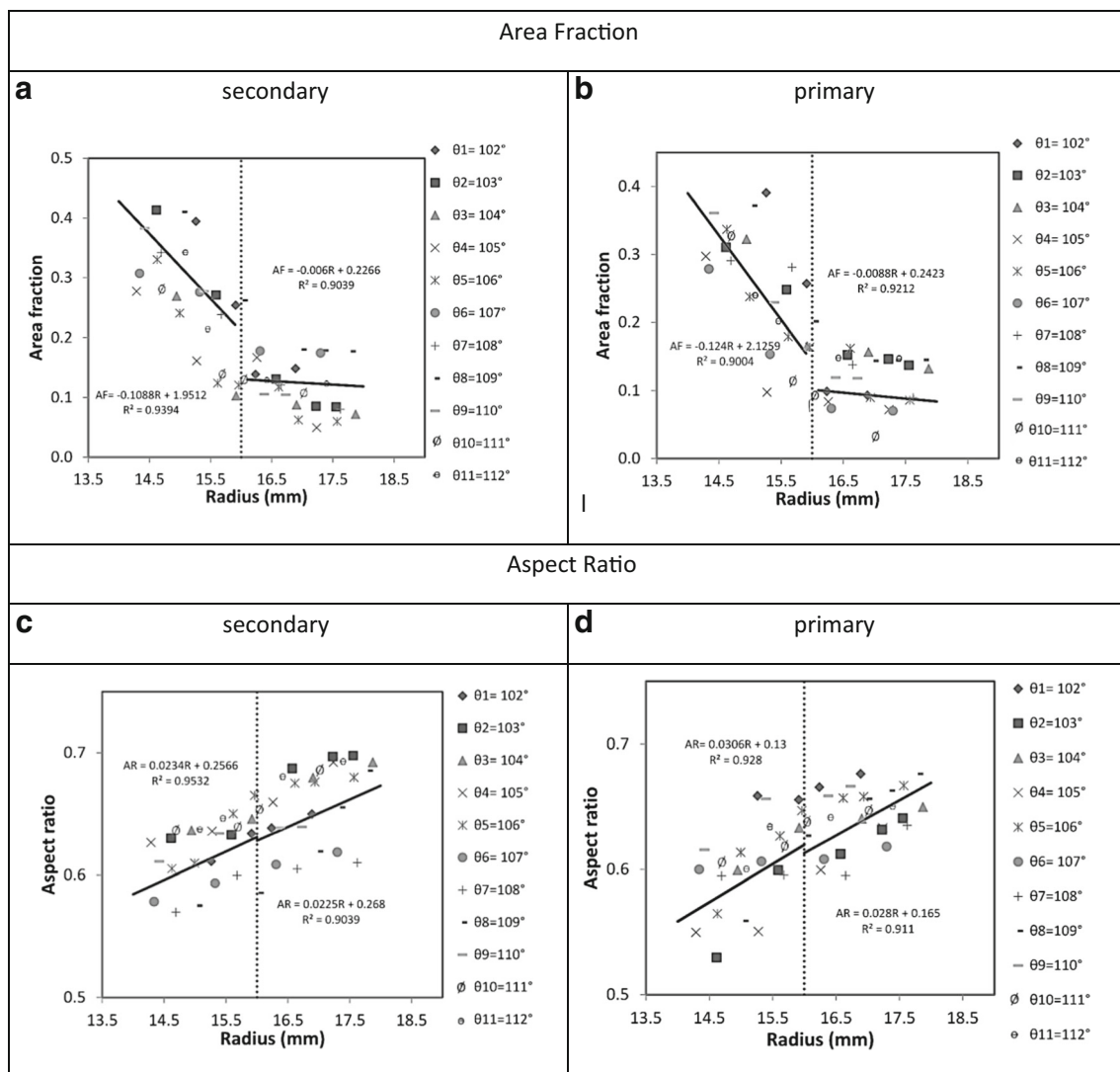


Fig. 5 Lacuna: area fraction (AF) plotted vs. radius in secondary and primary osteons area at all the angles: (a) secondary osteon (b) primary osteon; aspect ratio (AR) plotted vs. radius at all the angles (c) secondary osteon, (d) primary osteon

Calculated lacunae’ area fraction and aspect ratio values in each region are plotted versus radius, R , for all angles as shown in Fig. 5. Compared with AR values of bovine tibia found by Lin and Xu [4] for compact bone of bovine tibia of 0.4–0.4, values found here tend to be larger. Using atomic force microscope, Lin and Xu [4] determined the canaliculi diameter to be about half a micrometer and canaliculi density to be roughly 1 canaliculi feature per micrometer square. The lacunae were found to have non-uniform shapes with average lacuna lengths to be 9.66 and 10.9 μm in the transverse and radial directions, respectively, and average widths of 3.86 and 5.37 μm in the transverse and radial directions, respectively. These yield average values of aspect ratios

of 0.4 and 0.5 in the longitudinal and transverse directions, respectively.

3.2 Canaliculi

Area fraction (AF, %) values of areas of the canaliculi clusters in each region are calculated by dividing the sum of areas in secondary and primary regions by the sum of areas of said regions, respectively as shown in Eqs. 3 and 4.

$$AF_{so}^c = \frac{S(A_{so}^c)}{A_{so}} \tag{3}$$

$$AF_{po}^c = \frac{S(A_{po}^c)}{A_{po}} \tag{4}$$

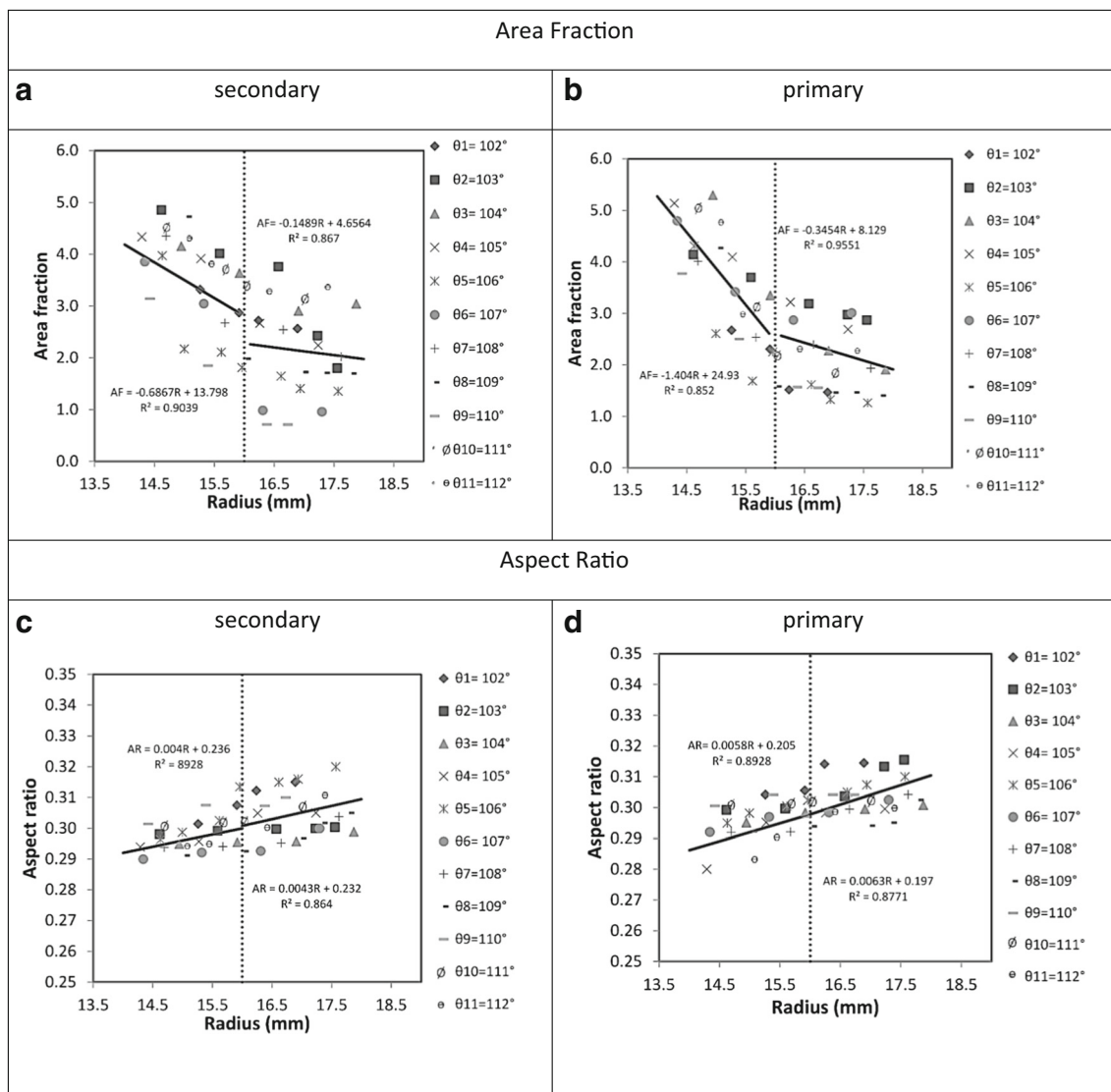


Fig. 6 Canaliculi clusters: area fraction (AF) plotted vs. radius in secondary and primary osteons area at all the angles: (a) secondary osteon (b) primary osteon; aspect ratio (AR) plotted vs. radius at all the angles (c) secondary osteon, (d) primary osteon

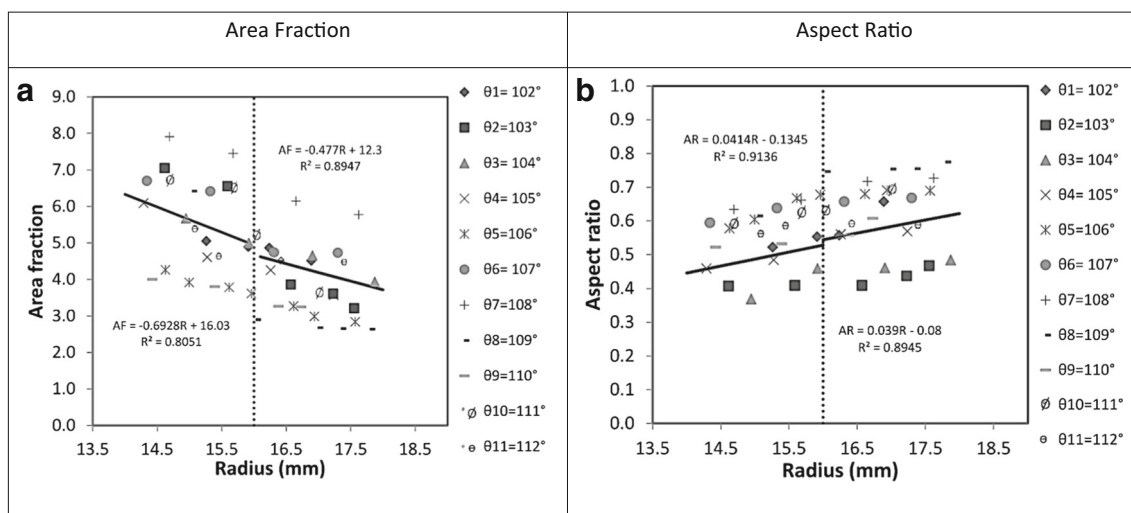


Fig. 7 Haversian canals: **a** area fraction (AF) and **b** aspect ratio (AR) plotted vs. radius in secondary osteons area at all the angles

The calculated values of canaliculi’ area fractions (%) and aspect ratio are plotted versus radius for all angles with the results shown in Fig. 6.

3.3 Haversian canals

The area fractions (%) of the Haversian canal areas in the secondary osteon are calculated by dividing the sum of Haversian canal areas in each region over the whole area of the secondary osteon as can be seen in Eq. 5.

$$AF_{so}^{hc} = \frac{S(A_{so}^{hc})}{A_{so}} \tag{5}$$

The calculated values of Haversian canals’ area fraction (%) and aspect ratio are plotted versus radius for all angles with the results shown in Fig. 7.

3.4 Resorption cavities

Since cortical bone contains (macro) porosity comprised of resorption cavities, primary osteons and the corresponding area fractional values of (any) resorption cavities in the image that contains the resorption cavity are calculated by dividing the sum of resorption cavity areas in each image by total area of the image as seen in Eq. 6.

$$AF^{rc} = \frac{A_{rc}}{(A_{so} + A_{po} + A_{rc})} = 1 - (\%so + \%po) \tag{6}$$

Note that if no resorption cavities exist in image, then (%so + %po) = 1. The resorption cavities’ area fractions (%) and aspect ratio are plotted versus *R* in Fig. 8. Each set represents the images that lie along the same angle where cavities were detected. Given that not all images contain resorption

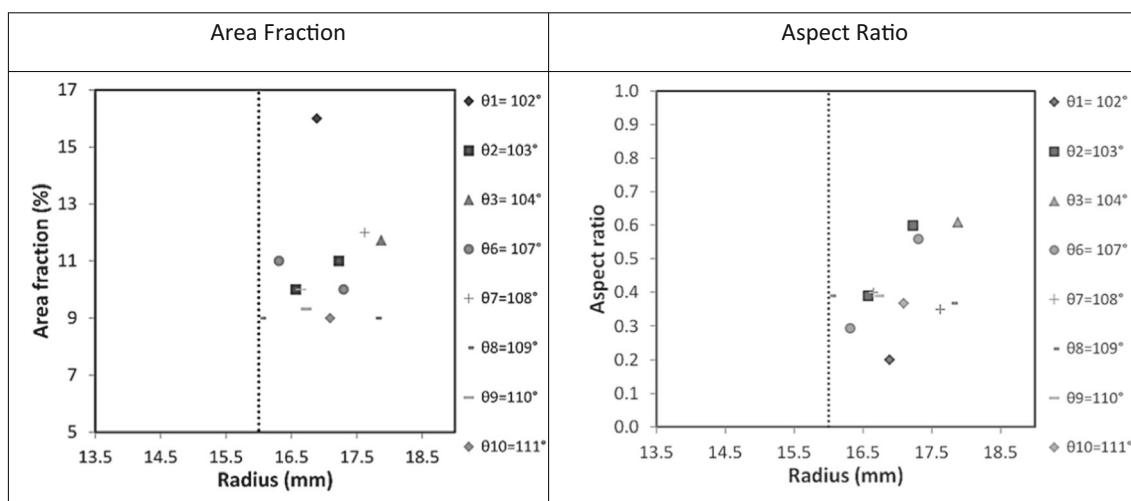


Fig. 8 **a** Area fraction (AF %) and **b** aspect ratio (AR) of resorption cavities plotted vs. radius at all angles

Table 1 Area fractions (%) and area fraction of lacunae in secondary and primary osteons, anterior and posterior regions: linear fits and statistics

	Area fraction		Aspect ratio	
Lacunae	Secondary osteon		Secondary osteon	
	Anterior	Posterior	Anterior	Posterior
Equation	$AF = -0.1088 \times R + 1.951$	$AF = -0.006 \times R + 0.226$	$AR = 0.0234 \times R + 0.2566$	$AR = 0.0225 \times R + 0.268$
<i>p</i> value	0.0065	0.001	0.0002	0.001
Lacunae	Primary osteon		Primary osteon	
	Anterior	Posterior	Anterior	Posterior
Equation	$AF = -0.124 \times R + 2.1259$	$AF = -0.0088 \times R + 0.242$	$AR = 0.0306 \times R + 0.13$	$AR = 0.028 \times R + 0.165$
<i>p</i> value	0.0011	0.0007	0.0005	0.0008

cavities, Fig. 8 suggests that no pattern is distinguishable for aspect ratios of these cavities versus R .

4 Discussion

4.1 Area fractions

In both posterior and anterior regions, the values of area fractions (%) plotted vs. radius R , in Fig. 5 (lacunae), Fig. 6 (canaliculi clusters), and Fig. 7 (Haversian canals), are fitted using linear ($f(x) = a * x + b$) best-fit trend lines. Tables 1, 2, and 3 list linear best-fit equations obtained for the lacunae, canaliculi clusters and Haversian canals, respectively.

Area fraction (%) values of all porosities decrease as distance from bone center increases from the midcortical toward the outer circumferential lamella regions (similar to findings by Thomas et al. [5, 6] and Hage and Hamade [15]). Area fractions (%) of the lacunae decrease linearly with R in both primary and secondary osteons in the anterior region. AF values appear to reach steady state in the posterior region. Area fractions (%) of the canaliculi clusters and Haversian canals also decrease linearly with R in primary and secondary osteons in the anterior region. They decrease at slower rate in the posterior region.

For all three pores, AF values decrease versus radius which may be related to osteonal growth in the anterior region. After building new bone, osteoblasts transform into osteoclasts and reside in lacunae and canaliculi. Remodeling process of bones causes areas of lacunae, canaliculi clusters, and Haversian canals to shrink in the anterior region, thus resulting in decrease in area fractions. The following observations can be made relating to findings in this work to others as reported in the literature and related to bone regeneration and remodeling.

4.1.1 In anterior regions

1. AF values of lacunae decrease with R due to strains generated during remodeling by the action of the resorbing cutting cone in the anterior region. Strains are largest at the base of the lacunae and smallest in surrounding bone (Clarke [21]) causing lacunae areas to shrink.
2. AF values of canaliculi clusters decrease with R due to bone remodeling activated in the anterior region through canalicular fluid flow (transporting nutrients causing channel areas to be larger). For larger R , bone remodeling is deactivated gradually requiring less fluid flow thus less canalicular channels activity and, consequently, reducing the size of channels (Zhou et al. [22]).

Table 2 Area fractions (%) of canaliculi clusters in secondary and primary osteons, anterior and posterior regions: linear fits and statistics

	Area fraction		Aspect ratio	
Canaliculi	Secondary osteon		Secondary osteon	
	Anterior	Posterior	Anterior	Posterior
Equation	$AF = -0.687 \times R + 13.798$	$AF = -0.1489 \times R + 4.656$	$AR = 0.004 \times R + 0.236$	$AR = 0.0043 \times R + 0.232$
<i>p</i> value	0.0009	0.007	0.0013	0.0024
Canaliculi	Primary osteon		Primary osteon	
	Anterior	Posterior	Anterior	Posterior
Equation	$AF = -1.404 \times R + 24.93$	$AF = -0.3454 \times R + 8.129$	$AR = 0.0058 \times R + 0.205$	$AR = 0.0063 \times R + 0.197$
<i>p</i> value	0.003	0.0008	0.0013	0.0019

Table 3 Area fractions (%) of Haversian canals in secondary and primary osteons, anterior and posterior regions: linear fits and statistics

Haversian canals	Area fraction		Aspect ratio	
	Anterior	Posterior	Anterior	Posterior
Equation	$AF = -0.693 \times R + 16.03$	$AF = -0.477 \times R + 12.3$	$AR = 0.0414 \times R - 0.1345$	$AR = 0.039 \times R - 0.08$
<i>p</i> value	0.0062	0.0043	0.0008	0.0013

3. AF values of Haversian canals decrease with *R* may be stimulated by the action of the cutting cone activated during bone remodeling in the anterior region. Large cylindrical canals are destroyed and concentric lamellae form around the Haversian canal starting from the outer to the inner diameter (Lerner [23]) that may cause the Haversian canals to shrink.

4.1.2 In posterior regions

1. Trends of lacunae’s AF are practically flat. As bone remodeling activities are reduced and osteons near completion, the rate of appositional bone formation slows causing lacunae areas to stabilize.
2. Canaliculi cluster’s AF values continue to decrease slightly versus *R*. Gradual deactivation of bone remodeling require less fluid flow, thus, fewer canaliculi channels activities (Zhou et al. [22]) causing channel areas to continue their slightly decreasing trend.
3. Haversian canals’ AF values continue to decrease slightly versus *R*. Younger remodeled Haversian systems are less completely mineralized (Thomas et al. [6]) than older ones. Even fully formed osteons require mineralization which is accomplished during progressive and continuing bone remodeling (Raisz [24]) in posterior regions, thus, causing Haversian canals on a continuing shrinking path.

4.2 Aspect ratios

The aspect ratio values versus radius, *R*, in Fig. 5 (lacunae), Fig. 6 (canaliculi clusters) and Fig. 7 (Haversian canals) are fitted using linear ($f(x) = a \times x + b$) best-fit trend lines in both posterior and anterior regions. Tables 1, 2, and 3 list the results of linear trend lines obtained for the lacunae, canaliculi clusters, and Haversian canals, respectively. Aspect ratios for all pores exhibit similar trends in anterior and posterior regions. These trends are fitted with linear trend lines versus *R* in both primary and secondary osteons. This increase of AR suggests that pores tend to become more rounded in the posterior region due to near completion of bone remodeling where matured osteons with circular pores are favored. Posterior regions

appear to contain nearly rounded osteons while anterior regions appear to be near ellipsoidal in agreement with Mayya et al. [20].

5 Conclusions

AI-based image segmentation methodology was utilized in this work where measures of area fraction (%) (AF) and aspect ratio (AR) of pores (namely, lacunae, canaliculi clusters in secondary and primary osteons, Haversian canals, and resorption cavities) are quantified in cortical bone as function of radius (*R*). Based on the data extracted, simple equations in AF and AR versus *R* are developed.

This work as accomplished by executing similar automated image analysis methodology developed by the authors (Hage and Hamade [12, 13, 15]). Images at × 20 magnification are captured in samples of the shell of bovine cortical bone biopsies containing both anterior (midcortical) and posterior (outer circumferential lamella) regions. Polar coordinates of center of these images are calculated from corresponding Cartesian (*x-y*) coordinates. Lacunae, canaliculi clusters, Haversian canals, and resorption pores are isolated in separate images. Values of AF and AR of each pore in each image are plotted against polar radius *R*.

Quantitative findings may be associated with established qualitative observations during osteonal remodeling and growth as follows:

1. For all pores (lacunae, canaliculi clusters, and Haversian canals) in anterior regions, area fractions (%) are found to diminish linearly (statistically significant $p < 0.01$) with *R* for both primary and secondary osteons. In posterior regions, a much slower decreasing trend is observed perhaps due to nearly completed osteon formation.
2. For all pores, in anterior and posterior regions, aspect ratios are found to increase linearly and at practically the same rates with *R* (statistically significant $p < 0.01$) in both primary and secondary osteons. This suggests that pores tend to become more circular at bone locations near the bone’s outer shell where mature and near-rounded osteons exist.

Acknowledgments This publication was made possible by Award #103087 from the Lebanese NCSR. The authors also acknowledge the support of the university research board (URB) at the American University of Beirut.

References

- Remaggi F, Cane V, Palumbo C, Ferretti M (1998) Histomorphometric study on the osteocyte lacuno-canalicular network in animals of different species. I. Woven-fibered and parallel-fibered bones. *Ital J Anat Embryol* 103:145–155
- Cardoso L, Fritton SP, Gailani G, Benalla M, Cowin SC (2013) Advances in the assessment of bone porosity, permeability, and interstitial fluid flow. *J Biomech* 46:253–265
- Wang X, Ni Q (2013) Determination of cortical bone porosity and pore size distribution using a low field pulsed NMR approach. *J Orthop Res* 21:312–319
- Lin Y, Xu S (2011) AFM analysis of the lacunar-canalicular network in demineralized compact bone. *J Microsc* 241:291–302
- Thomas CDL, Feik SA, Clement JG (2005) Regional variation of intracortical porosity in the midshaft of the human femur: age and sex differences. *J Anat* 206:115–125
- Thomas CDL, Feik SA, Clement JG (2006) Increase in pore area, and not pore density, is the main determinant in the development of porosity in human cortical bone. *J Anat* 209(2):219–230
- Bousson V, Meunier A, Bergot C, Vicaut É, Rocha MA, Morais MH, Laval-Jeantet A, Laredo J (2001) Distribution of intracortical porosity in human midfemoral cortex by age and gender. *J Bone Miner Res* 16(7):1308–1317
- Nirody JA, Cheng KP, Parrish RM, Burghardt AJ, Majumdar S, Link TM, Kazakia GJ (2015) Spatial distribution of intracortical porosity varies across age and sex. *Bone* 75:88–95
- Tjong W, Nirody J, Burghardt AJ, Carballido-Gamio J, Kazakia GJ (2014) Structural analysis of cortical porosity applied to HR-pQCT data. *Med Phys* 41(1):013701
- Burghardt AJ, Buie HR, Laib A, Majumdar S, Boyd SK (2010) Reproducibility of direct quantitative measures of cortical bone microarchitecture of the distal radius and tibia by HR-pQCT. *Bone* 4:519–528
- Stein M, Feik S, Thomas C, Clement J, Wark J (1999) An automated analysis of intracortical porosity in human femoral bone across age. *J Bone Miner Res* 14(4):624–632
- Hage IS, Hamade RF (2013) Segmentation of histology slides of cortical bone using pulse coupled neural networks optimized by particle-swarm optimization. *Comput Med Imaging Graphics* 7:466–474
- Hage IS, Hamade RF Toward quantifying geometric microstructural differences between primary and secondary osteons via segmentation, 2014 Middle East Conference on Biomedical Engineering (MECBME), February 17–20, 2014, Hilton Hotel, Doha, Qatar, IEEE 371–374
- Hage IS, Hamade RF. Distribution of porosity in cortical (bovine) bone, Proceedings of the ASME 2015 International Mechanical Engineering Congress & Exposition, IMECE2015, IMECE2015-51703, November 13–19, 2015, Houston, Texas
- Hage IS, Hamade RF (2016) Geometric-attributes-based segmentation of cortical bone slides using optimized neural networks. *J Bone Miner Metab* 34:251–265
- Hage IS, Hamade RF (2016) Detecting individual osteons in histology cortical bone slides using PSO-optimized PCNN. *AIMS Med Sci* 2:328–346
- Revell P (1983) Histomorphometry of bone. *J Clin Pathol* 12:1323–1331
- Lindblad T, Kinser J (2013) Image processing using pulse-coupled neural networks. Springer-Verlag, Berlin Heidelberg
- Gao K, Dong M, Jia F, Gao M OTSU image segmentation algorithm with immune computation optimized PCNN parameters. IEEE, Congress on Engineering and Technology (S-CET), 27–30 May 2012
- Mayya A, Banerjee A, Rajesh R (2013) Mammalian cortical bone in tension is non-Haversian. *Sci Rep* 3:Article number 2533
- Clarke B (2008) Normal bone anatomy and physiology. *Clin J Am Soc Nephrol Suppl* 3:S131–S139
- Zhou X, Novotny JE, Wang L (2009) Anatomic variations of the lacunar-canalicular system influence solute transport in bone. *Bone* 45(4):704–710
- Lerner UH (2012) Osteoblasts, osteoclasts, and osteocytes: unveiling their intimate-associated responses to applied orthodontic forces. *Semin Orthod* 18:237–248
- Raisz LG (1999) Physiology and pathophysiology of bone remodeling. *Clin Chem* 45(8 Pt 2):1353–1358



Dr. Ilige S. Hage is an assistant professor of Mechanical Engineering at Notre Dame University- Louaize in Zouk Mosbeh, Lebanon.



Dr. R. F. Hamade is a professor of Mechanical Engineering at the American University of Beirut in Beirut, Lebanon.